Numerical Methods in Civil Engineering, 8-3 (2024) 29-40

Numerical Methods in Civil Engineering

Journal Homepage: https://nmce.kntu.ac.ir/

Simulation of Wave and Non-Newtonian Mud Interaction using an ISPH Based on Modified Inter-Particle Average

Kourosh Hejazi[*], Mohsen Soltanpour[**], Abolfazl Aslani Kordkandi[***]

ARTICLE INFO

RESEARCH PAPER

Article history:
Received:
December 2023
Revised:
February 2024
Accepted:
April 2024

Keywords:
Modified ISPH method
Inter-particle average
Multiphase flow
Water-mud Interface
Wave attenuation
Mass transport velocity

Abstract:

Fluid mud is found in many areas, including coastal areas and river estuaries. The typical characteristics of overlaying waves interacting with muddy beds are mud mass transport and high wave attenuation (dissipation). In this study, an Incompressible Smoothed Particle Hydrodynamics (ISPH) method has been developed to simulate the interaction of wavesand non-Newtonian mud. A modified inter-particle average technique was used to solve the discontinuity through the interface. An iterative method was applied to update viscous force and to fulfill the requirement of the full incompressibility of the fluid. An improved formulation of viscous force terms, a new interface, and free-surface treatments have been presented. Some hydrodynamic tests were performed to verify the model by comparing the simulated results with analytical solutions. Several wave-mud simulations were carried out to investigate mass transport velocities and wave attenuation in the mud layer under the different wave and mud characteristics. To validate the results, the simulated results were compared with the laboratory measurements. The new modifications improve the force transferred from the surface wave into the fluid mud and enhance the simulated results in terms of the position of the particles, dissipation rate, and mud mass transport velocity. An intense gradient in the mass transport velocity is found at the water-mud interface.

1. Introduction

Fluid mud is found in many areas, including coastal areas and river estuaries. Fluid mud events are a serious threat to navigation safety because they can cause extreme siltation and complicate dredging and decrease in nautical depth [1, 2]. The typical characteristics of wave-mud interaction are the attenuation (dissipation) of the wave and the transport of mass in the bed layer. The attenuation of waves that propagate over muddy beds is significant for designing nearshore structures and for protective measures affairs on muddy coasts because, in these regions, the wave energy diminishes considerably so that nearly no wave breaking takes place.

Moreover, siltation and contaminant transport induced by the interaction of waves and mud are of great environmental and engineering importance [3]. The overlaying waves oscillate the mud particles in the fluid-mud layer, resulting in a steady current inside the fluid-mud layer, known as mud mass transport. While the magnitude of this current is small, it forms a large part of the total sediment transport. Several studies have investigated the wave-mud interaction during the past decades. Most of these studies were analytical and experimental [4-12]. Sakakiyama and Bijker [4] performed experiments using the water-kaolinite mixture which behaved like a Bingham fluid, to display surface wave attenuation and mass transport. The rheology of kaolinite and Hendijan mud was studied by Soltanpour and Samsami [5] to show the effect of mud on the dissipation of surface water waves. They found out that the rheological properties of mud are strongly site-specific. Hsu et al. [6] investigated mud transport induced by using an Electromagnetic Current Meter to measure particle velocity inside the fluid mud. Under the low-energy conditions, the wave nonlinearity was amplified due to non-Newtonian rheology. Soltanpour et al.

[*] *Corresponding Author: Assistant Professor, Faculty of Civil Engineering, K.N. Toosi University of Technology, Tehran, IRAN. Email: hejazik@kntu.ac.ir*

[**] *Professor, Faculty of Civil Engineering, K.N. Toosi University of Technology, Tehran, IRAN. Email: soltanpour@kntu.ac.ir*

[***] *PhD Candidate in Civil Engineering, K.N. Toosi University of Technology, Tehran, IRAN. Email: a.aslani@mail.kntu.ac.ir*

https://doi.org/10.52547/NMCE.2303.1042

[7] investigated wave dissipation and mud mass transport using ECM sensors in laboratory experiments. Shamsnia et al. [8] reviewed the literature investigating the wave-mud interactions and also compared their outputs with the available laboratory data of experiments. They also proposed a new model in the case of wave-mud and wave–current–mud interactions. Soltanpour et al. [9] studied a solitary wave-mud interaction by means of sets of laboratory tests. They measured time series of the velocity in the water and mud layers, as well as free-surface evolutions. At higher values of the mud water content ratio, the time shifts decrease between the peak velocities in the mud and water layers. Quesada et al. [10] studied analytically the damping of long linear waves propagating on a thin mud layer, with viscoelastic behavior using the well-known Maxwell rheological model. Kamrooz et al. [11] provided a straightforward analytical solution to wave-current-mud interaction by considering the mean shear stress effects in the water layer in contrast to the abundance of experimental and analytical research, very few numerical models have been presented in the literature concerning the simulation of the wave and mud interaction. A 2DV numerical model based on an ALE description was developed by Hejazi et al. [12] for the simulation of wave propagation over Newtonian mud layers.

SPH, as the most advanced member of Lagrangian methods, is a great alternative to simulate complex flow problems due to some distinct preferences. For example, it remarkably simplifies the tracking of free-surface and interface particles, as well as moving boundaries. It also enables modeling the large deformations in flows, facilitates the combination of interfacial forces into momentum equations, and does not need a mesh to calculate partial differential terms in governing equations [13]. Therefore, SPH methods can overcome limitations related to mesh-based methods and provide accurate results in the simulation of free-surface and interface problems. In problems that deal with several different fluids, due to the difference in their density and viscosity, a discontinuity occurs at the interface, which requires special consideration in calculating the derivatives [14]. Several studies have been carried out on multiphase flows. Hu and Adams [15, 16] proposed an inter-particle averaged value method in the multiphase SPH methods. The new method was capable of handling the discontinuity across the interface. However, they assumed that the interface was exactly between the two particles of two different fluids. This assumption disregards the real particle distance from the interface and obtains the inter-particle pressure based on the weighted average according to their densities. In practice, most of the time, the interface is not placed exactly between the two particles and this issue makes some errors. Therefore, it is necessary to estimate the distance of the two particles from the exact interface. Also, this method has not been developed for free problems, which needs to extract relations for the free surface.

In sediment transport and coastal engineering problems, Granular material approaches have been applied newly [17-21]. Continuum approaches have also been employed in which the granular materials are considered a fluid body and the laboratory experiments determine the effects of these materials on the parameters of the fluid rheological models. Some researchers found out in their laboratory studies that bed sediments have the Bingham plastic behavior [1, 6]. This rheological model has been recently used for the mud bed in simulating the wave and mud interaction [3, 22-24].

Hejazi et al. [3] presented a modified ISPH model with a new kernel function for simulating the interaction between waves and fluid mud. They used Bingham's model to describe the behavior of mud. This simple model, which preserves the basic behavior of mud, facilitates the application of SPH method [3]. Many relations for calculating shear stress have been presented in the literature. However, there is a need an alternative approach to calculating shear stress.

In the present study, to solve the problem of discontinuity through the interface in thesimulation of the wave and non-Newtonian mud interaction, an ISPH method based on an enhanced inter-particle average was developed in which mud was considered as a continuum body. An iterative method has been employed to fulfill the requirement of the full incompressibility of ISPH. Free-surface relations were derived, and a modified interface treatment was proposed. The ISPH formulation of the shear stress in the governing equations was discussed in detail and an improved method was offered. Some hydrodynamic tests were carried out to verify the simulation by comparing them with the analytical solutions. Themud mass transport velocity and the attenuation of waves passing over the mud layer were predicted and a comparison was made with the results obtained from the related experiments and theoretical solutions reported in the literature.

2. Solution method

The 2D governing equations for incompressible flow are expressed as [16, 25]:

$$\frac{1}{\rho}\frac{\mathrm{D}\rho}{\mathrm{D}t}+\nabla.\vec{U}=0 \tag{1}$$

$$\frac{\mathrm{D}\vec{U}}{\mathrm{D}t}=-\frac{1}{\rho}\nabla P+\vec{g}+\frac{1}{\rho}\nabla.\vec{\vec{\tau}}+\frac{1}{\rho}f_s \tag{2}$$

where ρ denotes the density, t is time, $\vec{U}$ is the vector of velocity, P is the pressure, $\vec{g}$ is the vector of gravitational

acceleration, $\vec{\tau}$ is the tensor of viscous force and f_s is the surface stress expressed as [13]:

$$f_s = -\alpha \nabla . \left(\frac{\nabla C}{|\nabla C|} \right) \nabla C \tag{3}$$

where α is the surface-tension coefficient and C is the color index, which ranges between 0 and 1 [16]. The particle density can be obtained from $\rho_i = m_i \sigma_i$ which conserves mass exactly, m_i is the particle mass and the particle number density σ_i is almost the inverse of the particle volume. The subscript i is the particle on which the calculation is performed. The vital equation by which the other formulation of the inter-particle averaged value method can be derived is the gradient of a scalar function defined as [16]:

$$\nabla \psi_i \approx \sigma_i \sum_j \left(\frac{1}{\sigma_i^2} + \frac{1}{\sigma_j^2} \right) \overline{\psi}_{ij} \frac{\partial W_{ij}}{\partial r_{ij}} \vec{\boldsymbol{e}}_{ij} = \sigma_i \sum_j A_{ij} \overline{\psi}_{ij} \vec{\boldsymbol{e}}_{ij}$$
$$A_{ij} = \left(\frac{1}{\sigma_i^2} + \frac{1}{\sigma_j^2} \right) \frac{\partial W_{ij}}{\partial r_{ij}} \tag{4}$$

where W denotes the kernel function.

The $\overline{\psi}_{ij}$ is the inter-particle average, which is often an arithmetic mean $\frac{\psi_i + \psi_j}{2}$, and $\vec{\boldsymbol{e}}_{ij}$ is the unit vector from particle i to neighboring particle j and $\vec{r}_{ij} = \vec{r}_i - \vec{r}_j = r_{ij} \vec{\boldsymbol{e}}_{ij}$. Accordingly, discretization of second-order derivative (Laplacian) is written as:

$$\nabla . \nabla \psi_i \approx \sigma_i \sum_j A_{ij} \frac{\psi_{ij}}{r_{ij}} \tag{5}$$

where $\psi_{ij} = \psi_i - \psi_j$. A projection method was utilized in solving the governing equations to fulfill the requirement of the full incompressibility of ISPH. For detailed information on implementing this method, the readers can refer to [3, 16]. To solve the problem of discontinuity of density and viscosity across the interface, Hu and Adams [15, 16] supposed that the interface is situated exactly in the middle of two particles belonging to the two different fluids A and B and accordingly discretize discretized the pressure gradient as:

$$\langle \nabla P / \rho \rangle_i = \frac{1}{m_i} \sum_j A_{ij} \frac{\rho_i P_j + \rho_j P_i}{\rho_i + \rho_j} \boldsymbol{e}_{ij} \tag{6}$$

where the inter-particle pressure becomes:

$$P_m = \frac{P_j \ \rho_i + P_i \ \rho_j}{\rho_i + \rho_j} \tag{7}$$

And the inter-particle velocity can be written as:

$$v_m = \frac{\mu_i v_i + \mu_j v_j}{\mu_i + \mu_j} \tag{8}$$

where v is velocity and μ is viscosity. For the two particles belonging to the same fluid, the inter-particle pressure and velocity become $P_m = \frac{P_i + P_j}{2}$ and $v_m = \frac{v_i + v_j}{2}$ respectively. The Poisson operator is discretized as:

$$\langle \nabla . (\nabla P / \rho) \rangle_i = 2 \sigma_i \sum_j \frac{A_{ij}}{r_{ij}} \frac{P_{ij}}{\rho_i + \rho_j} \tag{9}$$

The discretization form of the Poisson equation will be:

$$\sum_j \frac{2 A_{ij}}{r_{ij}} \frac{P_{ij}}{\rho_i + \rho_j} = \frac{1}{\Delta t} \sum_j A_{ij} \left(\frac{\mu_i v^*_i + \mu_j v^*_j}{\mu_i + \mu_j} \right) . \boldsymbol{e}_{ij} \tag{10}$$

The right side of equation (10) is based on the divergence-free equation, and the superscript (*) denotes the intermediate step. In this study, the Sparse-Gauss–Seidel (SGS) solver, which is an iterative technique, using a successive over-relaxation (SOR) accelerator was employed to solve the pressure Poisson equation for finding particle pressure. The factor of relaxation varies from 1.85 to 1.96. The convergence condition to stop the iterative process was $\max \left| P^{n+1} - P^n \right| \le 10^{-6}$ where P^{n+1} and P^n are the Successive pressure in the iterative process. The great benefit of this technique is that there is no need to create a huge 2D matrix for the pressure Poisson equations, and subsequently, a small amount of computer memory is occupied so that even a simple PC can handle simulation with a large number of particles. To determine the time step, the following constraints must be satisfied:

$$\Delta t \le \min \left(0.1 \frac{L_0}{U_{max}} , \alpha \frac{L_0^2}{\mu / \rho} \right) \tag{11}$$

The first constraint is related to the maximum movement of particles and viscous diffusion determines the second constraint on the time step. U_{max} denotes the maximum velocity of particles in the computation and L_0 is the initial spacing of particles. α , usually in the order of 0.1, is the coefficient depending on the particle arrangement and the type of the Kernel function. To fulfill the requirement of the complete incompressibility of the fluid, the corrected position and velocities of particles are considered as intermediate values again, and an iterative process is made to obtain ΔP and ΔU, the pressure and velocity increments, to correct the new pressure and velocity (equation 12). In the following equations, the subscripts .show the iteration number

$$P_2 = P_1 + \Delta P$$
$$\vec{U}_2^{\,n+1} = \vec{U}_1^{\,n+1} + \Delta U \qquad (12)$$
$$\vec{r}_2^{\,n+1} = \vec{r}^{\,n} + \frac{\vec{U}^{n} + \vec{U}_2^{\,n+1}}{2}\Delta t$$

Two correction factors were used for velocity in the model to rearrange the position of the particles after correction steps. The first correction factor, or XSPH correction, proposed by Monaghan [26] is added to the velocity of the particles to keep the particles more regular and to prevent the penetration of particles into each other, especially in high-speed flow. The corrected velocity of particles conserves the linear and angular momentum [26]. Another method to control particle regulation is the particle collision technique. This method is defined as follows [27]:

$$v_i = u_i - \frac{m_i}{m_i + m_j}(1 + C_R)\frac{(u_{ij} . r_{ij})\, r_{ij}}{\left|r_{ij}\right|^2} \qquad (13)$$

where C_R ranges between 0 and 1, indicating non-elastic and elastic collision, respectively. v_i and u_i stand for the velocity with and without modification of the particle collision respectively. The summation of all neighboring particles situated in the collision distance ($C_i = 0.75 L_0$) is gained by equation 14.

$$v_i = u_i - \sum_{b \in C_i} \frac{m_i}{m_i + m_j}(1 + C_R)\frac{(u_{ij} . r_{ij})\, r_{ij}}{\left|r_{ij}\right|^2} \qquad (14)$$

3. Boundary conditions

In this section, three types of boundary conditions have been presented which are the free-surface, the interface and the wall boundary conditions. For the simulation of free-surface flows, it is necessary to use suitable formulations for the free-surface particles. In the studies carried out by Hu and Adams [15, 16], the inter-particle averaged values were used for multiphase problems involving interfaces in confined containers, but no treatment was provided for the free-surface problems. Furthermore, the existing relations for the interface were obtained based on the assumption that the imaginary interface was located in the middle of two particles belonging to the two different fluids, which requires that the effects of particles close to the actual interface are equal to the effect of the further ones. The appropriate relationships are presented in this section to address the two mentioned shortcomings.

3.1 Free-surface treatment with modification

Similar to formulations used for free-surface treatment in the ISPH model proposed by [3, 28], here, the formulations are derived for the inter-particle averaged method. Figure 1 shows a typical free-surface particle. The particles that meet the following criteria are treated as free-surface particles:

$$\rho^* \le \gamma\, \rho_0 \qquad (15)$$

where γ = constant (= 0.9 to 0.98 in this study). Since inside the support domain, the neighboring particles for each free-surface particle are deficient, the particle density decreases over the free-surface boundary, consequently causing a false pressure gradient. The condition of zero pressure is applied to the free-surface particles. The gradient of pressure among the free-surface particles, inner particle (i) and mirror particle (m) (Figure 1) is derived as:

$$\left(\frac{\nabla P}{\rho}\right)_s = \frac{1}{m_i}\sum_i A_{si}\, \bar{P}_{si}\, e_{si} = \frac{2}{m_i}\sum_i A_{si}\, P_i\, e_{si} \qquad (16)$$

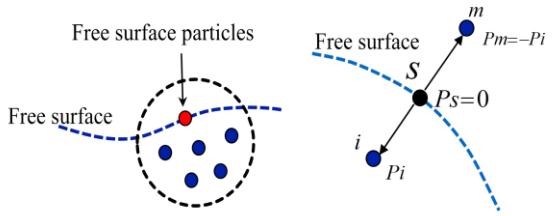

Fig. 1: Schematic diagram for free-surface formulation using virtual mirror particles

Similarly, the Poisson equation of pressure is expressed as:

$$\left\langle \nabla . (\nabla P/\rho) \right\rangle_s = 2\sigma_i \sum_i \frac{A_{si}}{r_{si}} \frac{2P_s}{\rho_i + \rho_s} \qquad (17)$$

The factor of free-surface curvature for the gradient and Poisson of pressure are applied as [3]:

$$\left\langle \Delta P/\rho \right\rangle_s = \frac{2}{m_i} \frac{\sum_j W_{ij\text{-}std}}{\sum_j W_{ij}} \sum_i A_{si}\, P_i\, e_{si} \qquad (18)$$

$$\left\langle \nabla . (\nabla P/\rho) \right\rangle_s = 2 \frac{\sum_j W_{ij-std}}{\sum_j W_{ij}} \sigma_i \sum_i \frac{A_{si}}{r_{si}} \frac{2P_s}{\rho_i + \rho_s} \qquad (19)$$

3.2 Modification in the interface relation

In this study, it is assumed that there is a sharp interface between the water and mud layers and there is no considerable mixing between water and mud. As mentioned, the imaginary interface was located just in the middle of two particles in fluids A and B. As seen in Figure 2, this assumption neglects the actual distance of the particle from the interface position and it obtains the inter-particle pressure based on the weighted average according to their densities (Equation 7). In practice, most of the time, the interface is not placed exactly between the two particles, and this issue makes some errors. Therefore, it is necessary to

estimate the distance of the two particles from the exact interface. In order to locate the interface, a color function is used and it is assumed that the interface has a negligible curve. This assumption comes from the fact that the height of the internal wave is a small fraction of the surface wave height and can be considered a flat line in this study.

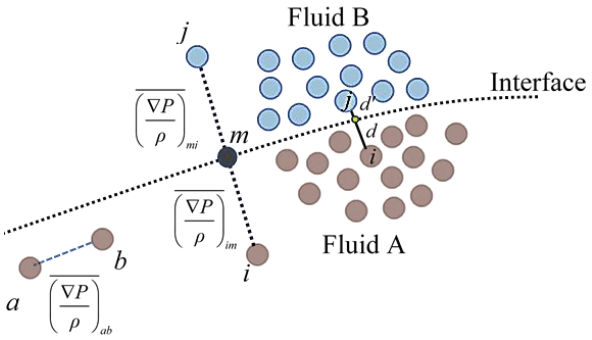

Fig. 2: A sketch of interface boundary condition for calculation of pressure gradient

The following coefficients are assigned for the particles of two fluids:

$$\hat{C}_i = \begin{cases} 1, & \text{in fluid A} \\ 0, & \text{in fluid B} \end{cases} \tag{20}$$

The color function is defined as the following relation:

$$C_i = \frac{\sum_j \hat{C}_i W_{ij}}{\sum_j W_{ij}} \tag{21}$$

If d and d' denote the distance of particles i and j from the actual interface, respectively, the ratio of the distances of d and d' is expressed as:

$$\frac{d'}{d} = \frac{0.5 - C_j}{C_i - 0.5} = k \tag{22}$$

The estimation of the ratio of the distances has been obtained from Figure 3.

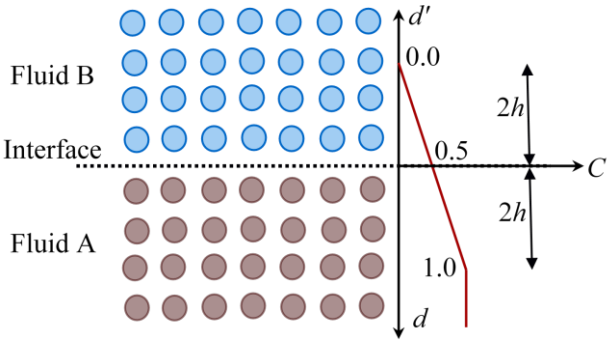

Fig. 3: A sketch of the interface for the calculation of color function and estimation of the distance ratio

Applying the coefficient on the equation of pressure gradient and pressure Poisson equation, the new equations are modified as:

$$\langle \Delta P/\rho \rangle_i = \frac{1}{m_i} \sum_j A_{ij} \frac{k\,\rho_i P_j + \rho_j P_i}{k\,\rho_i + \rho_j}\, e_{ij} \tag{23}$$

$$\langle \nabla.(\nabla P/\rho) \rangle_i = (1+k)\,\sigma_i \sum_j \frac{A_{ij}}{r_{ij}} \frac{P_{ij}}{k\,\rho_i + \rho_j} \tag{24}$$

The inter-particle averaged pressure is modified to:

$$P_m = \frac{k\,\rho_i P_j + \rho_j P_i}{k\,\rho_i + \rho_j} \tag{25}$$

The inter-particle-averaged velocity is also expressed as:

$$v_m = \frac{k\,\mu_i v_i + \mu_j v_j}{k\,\mu_i + \mu_j} \tag{26}$$

These formulations can partly deal with the problem raised in the large density ratio, in which denser fluid has less effect on lighter fluid as reported by Chen et al. [29]. However, due to the low-density ratio of the two fluids, this problem does not arise in the current model.

3.3 Boundary condition of the wall

In this study, the Neumann boundary condition was set to the wall particles. To set the wall boundary condition, a row of stationary particles was employed as a solid boundary, and two rows of fixed artificial particles were placed on the outer side of the solid boundary. In the pressure Poisson equation, only the boundary particles took part and the artificial particles were used to provide sufficient particles and apply a repulsive force on the approaching particles.

4. ISPH Kernel function

Several popular kernel functions have been checked, such as cubic spline, hyperbolic, double cosine, Wendland, and the new hybrid proposed by Hejazi et al. [3], and the proposed hybrid kernel function was chosen in the present model, mainly because it showed long-lasting stability in the simulations. The hybrid kernel function is expressed as:

$$W_{Hybrid}(r,h) = \alpha\, W_S(r,h) + (1-\alpha)\, W_H(r,h) \tag{27}$$

where W_S is the cubic spline, W_H is the hyperbolic kernel function and, α is a coefficient varying from 0 to 0.2, and h is the smoothing length. The radius of the support domain is $2h$ beyond which the value of the kernel function becomes zero.

5. Rheological equations

The water was regarded as Newtonian fluid in the present study, but a non-Newtonian fluid with the rheological model of Bingham is used for representing the mud behavior as follows:

$$\begin{cases} \dot{\gamma} = 0 & \underline{\underline{\tau}} \geq \tau_y \\ (\mu_B + \frac{\tau_y}{\underline{\underline{\dot{\gamma}}}})\,\dot{\gamma} & \underline{\underline{\tau}} < \tau_y \end{cases} \tag{28}$$

where $\dot{\gamma}$ is the shear strain rate tensor, τ_y is Bingham yield stress, μ_B is the Bingham viscosity. $\underline{\underline{\tau}}$ stands for the magnitude of shear stress and $\underline{\underline{\dot{\gamma}}}$ is the magnitude of shear strain rate expressed as:

$$\underline{\underline{\dot{\gamma}}} = \sqrt{2\left(\frac{\partial u}{\partial x}\right)^2 + 2\left(\frac{\partial w}{\partial z}\right)^2 + \left(\frac{\partial u}{\partial z} + \frac{\partial w}{\partial x}\right)^2} \tag{29}$$

The partial strain rates in equation (29) are derived from the finite difference method. For example, $\frac{\partial u}{\partial x}$ and $\frac{\partial u}{\partial z}$ are defined as:

The equation (32) describes the viscosity force in SPH [30].

$$\left.\frac{\partial u}{\partial x}\right|_i = \frac{\partial u}{\partial r} \times \frac{\partial r}{\partial x} = \frac{u_i - u_j}{r_{ij}} \times \frac{x_i - x_j}{r_{ij}} \tag{30}$$

$$\left.\frac{\partial u}{\partial z}\right|_i = \frac{\partial u}{\partial r} \times \frac{\partial r}{\partial z} = \frac{u_i - u_j}{r_{ij}} \times \frac{z_i - z_j}{r_{ij}} \tag{31}$$

If the neighboring particle is a water particle, the viscous force is applied using the constant viscosity; otherwise, the Bingham model is used to calculate the inconstant viscosity.

$$\left(\frac{1}{\rho}\nabla.\tau\right)_i = \sum_j \frac{8 m_j \mu_j}{(\rho_i + \rho_j)^2} \begin{bmatrix} \frac{\partial u}{\partial x} & \frac{1}{2}\left(\frac{\partial u}{\partial z} + \frac{\partial w}{\partial x}\right) \\ \frac{1}{2}\left(\frac{\partial u}{\partial z} + \frac{\partial w}{\partial x}\right) & \frac{\partial w}{\partial z} \end{bmatrix}_{i:j} \cdot \nabla_i W_{ij} \tag{32}$$

In the form of the inter-particle averaged method, this equation is rewritten as:

$$\left(\frac{1}{\rho}\nabla.\tau\right)_i = \sum_j \frac{2\bar{\mu} A_{ij}}{m_i} \begin{bmatrix} \frac{\partial u}{\partial x} & \frac{1}{2}\left(\frac{\partial u}{\partial z} + \frac{\partial w}{\partial x}\right) \\ \frac{1}{2}\left(\frac{\partial u}{\partial z} + \frac{\partial w}{\partial x}\right) & \frac{\partial w}{\partial z} \end{bmatrix}_{i:j} .e_{ij} \tag{33}$$

where $\bar{\mu} = \frac{k\mu_i + \mu_j}{1+k}$ and when the two particles belong to the same fluid it becomes a simple average $\bar{\mu} = \frac{\mu_i + \mu_j}{2}$.

The downside of the mentioned viscosity function model (Bingham model) is that the viscosity is discontinuous at the lower strain rate, and one must impose a large value instead of the infinity, which may cause a numerical instability in the lower shear strain rate region and cannot be used straight in the numerical simulation. To handle this discontinuity, the relationship provided by Papanastasiou [31] is used, which relates continuously the changes of shear stress to the strain rates as follows:

$$\tau = \mu_B \dot{\gamma} + \tau_y \left(1 - e^{-m\underline{\underline{\dot{\gamma}}}}\right) \tag{34}$$

where m adjusts the exponential growth of shear stress so that in m=0, the behavior of Newtonian fluid and in m larger than 500, the behavior of Bingham's fluid can be simulated ideally (Figure 4(a)). A correction matrix L is just multiplied by the viscosity term in order to guarantee the conservation of linear and angular momentum [32].

$$L_i = \left(\sum_b \frac{m_b}{\rho_b} \nabla_a W_{ab} \otimes (r_b - r_a)\right)^{-1} \tag{35}$$

5.1 New approach in calculation of shear stress

In the ISPH method, since all the neighboring particles inside the support domain take part in the calculation of the shear stress for the central particle *i*, it would be better to simultaneously calculate the effect of all neighboring particles (*j*) within the support domain of Ω on determining the magnitude of shear rates (Figure 4 (b) (II)). Because the pairwise calculation of the shear rates magnitude of the particle *i* with each *j* particle (Figure 4 (b) (I)) and then the calculation of shear stress of the particle *i* cannot solely indicate the moving situation of particle *i* and it is necessary that the accumulated effects of neighboring particles on the central particle are considered and then the effect of each neighboring particle is calculated separately proportional to the values of its strain tensor. For example, the longitudinal and transverse strain rates in the equation of total $\underline{\underline{\dot{\gamma}}}$ are calculated as follows:

$$\left.\frac{\partial u}{\partial x}\right|_i = \sum_{j=1}^{k}\left(\frac{\partial u_{ij}}{\partial r_{ij}}\frac{\partial r_{ij}}{\partial x_{ij}}\right) = \sum_{j=1}^{k}\left(\frac{u_i - u_j}{r_{ij}}\frac{x_i - x_j}{r_{ij}}\right) \tag{36}$$

$$\left.\frac{\partial w}{\partial z}\right|_i = \sum_{j=1}^{k}\left(\frac{\partial w_{ij}}{\partial r_{ij}}\frac{\partial r_{ij}}{\partial z_{ij}}\right) = \sum_{j=1}^{k}\left(\frac{w_i - w_j}{r_{ij}}\frac{z_i - z_j}{r_{ij}}\right) \tag{37}$$

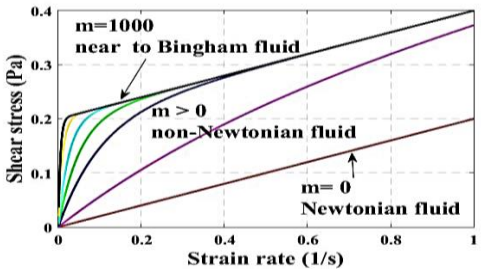

(a)

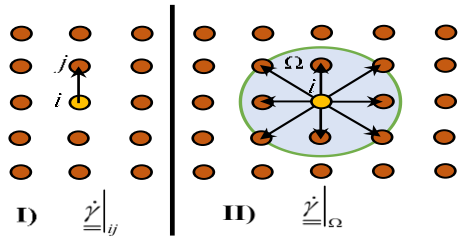

(b)

Fig. 4: (a): Papanastasiou model with different *m* (b) two approaches for calculation of the magnitude of shear rate (I): pairwise calculation and (II): simultaneously calculation of all particles inside the support domain

An alternative method for defining the equations 36 and 37 is obtained from velocity gradient definition in SPH as:

$$\left.\frac{\partial u}{\partial x}\right|_i = \sum_j \frac{m_j}{\rho_j}\left(u_j - u_i\right).\frac{\partial W_{ij}}{\partial x_{ij}} \tag{38}$$

$$\left.\frac{\partial w}{\partial z}\right|_i = \sum_j \frac{m_j}{\rho_j}\left(w_j - w_i\right).\frac{\partial W_{ij}}{\partial z_{ij}} \tag{39}$$

The following relation is expressed to describe the viscosity force in ISPH. If the neighboring particle is a water particle, the viscous force is calculated using the constant viscosity (μ) otherwise, the Bingham-Papanastasiou model is used with inconstant viscosity (μ_{BP}).

$$\left.\frac{1}{\rho}\nabla.\vec{\tau}\right|_i = \sum_j 8 m_j \left(\frac{\mu_j \quad \text{or} \quad \left(\mu_{BP}\right)_j}{(\rho_i+\rho_j)^2}\right).\dot{\gamma}|_{ij}.\nabla_i W_{ij}$$
$$\mu_{BP} = \mu_B + \frac{\tau_y}{\left.\dot{\gamma}\right|_{=\Omega}}\left(1-\exp\left(-m\left.\dot{\gamma}\right|_{=\Omega}\right)\right) \tag{40}$$

6. Model verification

For hydrodynamic verification of the present ISPH model, the simulation of the sinusoidal and solitary wave propagation was compared with the analytical results. In another numerical test, static water-mud layers were simulated to investigate the performance of the modified treatments. This model was written using Fortran programming language. The program was run using a laptop with RAM 16 GB and an Intel(R) Core (TM) i7-4720HQ CPU @ 2.60 GHz.

6.1 Sinusoidal and solitary wave propagation

The first test to validate the current model was the simulation of sine wave propagation. This simulation was conducted in a domain of 10 m length, with a wave generator at the entrance of the domain and a wave absorber at the end of it. The water depth was 0.2 m, the wave height was 4 cm, and the wave period was 0.87 s. The second test for the model's validity was the simulation of solitary wave propagation over a constant water depth. The wave amplitude was 3 cm and the water depth was adopted 10 cm. The analytical solution for the wave profile has been presented by Boussinesq [33] as:

$$\eta(x,t) = a\ \sec h^2[\sqrt{\frac{3a}{4d^3}}(x-ct)] \tag{41}$$

where η is water surface elevation, a is wave amplitude, d is water depth and $c = (\sqrt{g(d+a)}$ is the solitary wave celerity. The horizontal velocity underneath the wave profile is given by:

$$u = \eta\sqrt{\frac{g}{d}} \tag{42}$$

The analytical solution for the wave profile (η) can be derived from the following equation [34]:

$$\eta = \frac{H}{2}\cos\left(kx-\omega t\right) \tag{43}$$

Where *k* is the wave number equal to $\left(2\pi/L\right)$, *L* is the wave length, ω is the frequency of wave $\left(2\pi/T\right)$, *T*=wave period. Figure 5 displays the simulated results of both wave propagations compared with the analytical solutions.

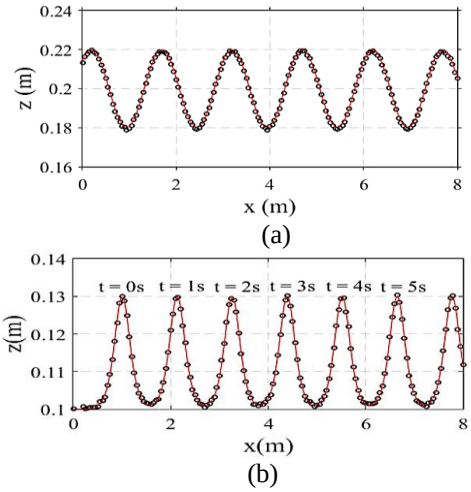

(a)

(b)

Fig. 5: Simulated results (circles) of (a) sinusoidal and (b) solitary wave propagations in comparison with the analytical solutions (solid lines)

6.2 Still water and mud layers

To evaluate the impact of the modified treatments on the interface and free-surface simulation, the simulation of a still water-mud system was carried out. Since the primary purpose of the study is to demonstrate wave attenuating over a muddy bed, still water-mud tests are essential. They confirm that the free-surface variations due to the errors, that may occur in the computations, have negligible effects on free-surface particles in the present numerical results.

Furthermore, the ability of the model in the hydrostatic-pressure prediction is examined. A confined domain with a length of 1m, overlying water layer depth of 0.1 m, and mud layer depth of 0.1 m were adopted for this test. Water and mud density were equal to 1000 kg/m³ and 1240 kg/m³, respectively. Figure 6 shows the position of particles for the still water-mud test at time 10s for both cases with and without the modified treatments. As can be seen in the figure, the modifications made have improved the position of the particles and their fluctuations have decreased.

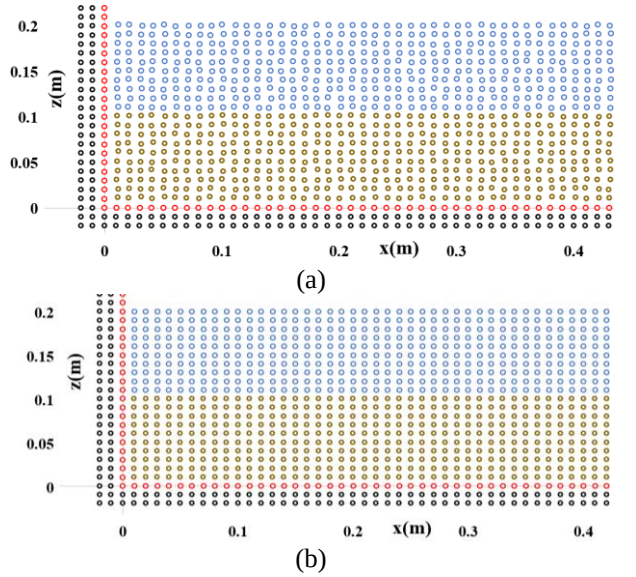

(a)

(b)

Fig. 6: Simulation of a still water-mud system, Position of the flow particles (blue circles), boundary particles (red circles), mud particles (brown circles), and artificial particles (black circles) at t=10s; (a) without modification, (b) with modification

The pressure contours (kPa) in the simulation of the still water-mud system at t=10s are shown in Figure 7 for both cases with and without the modified treatments. As seen in this figure, the corrections made have reduced the distortion of the pressure contour lines, and as a result, the accuracy of the simulation has increased.

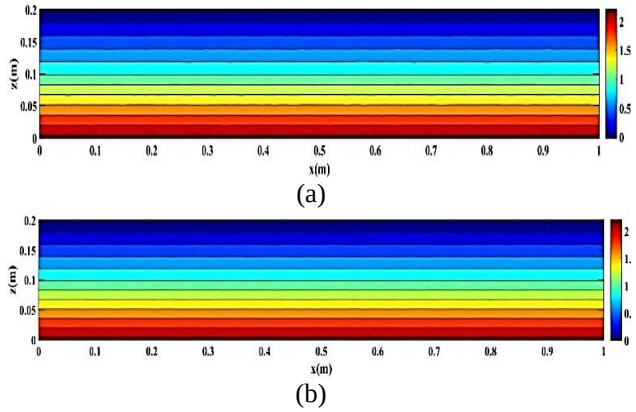

(a)

(b)

Fig. 7: pressure contours (kPa) in the simulation of the still water-mud system at t=10s; (a) without modified treatments, (b) with modified treatments

Since the primary test of wave-mud interaction takes 10-15 s, the still water-mud test was also simulated in this range. The variations of free-surface and interface particles are calculated by RMSE using equation (44).

$$\mathrm{RMSE}=\sqrt{\frac{\sum_{n}(0.5-z)^2}{n}} \tag{44}$$

where z is the height, and n is the total number of the particles considered as water surface and interface particles. Table 1 presents several errors made in the simulation of the still water-mud system with and without modifications. The errors associated with the density and pressure of particles were calculated using the analytical solutions. According to Table 1, the use of modified treatments has reduced the free-surface and interface fluctuations and also improved the simulated pressure of mud particles.

Table 1: Errors made in the simulation of a still water-mud system with and without the modifications

Interface treatment	position errors		
	Free surface (m)	Interface (m)	All particles (m)
Before	0.00033	0.00006	0.0003
After	0.00033	0.00004	0.00025
	Density and pressure errors		
Interface treatment	Density water (%)	Density mud (%)	Pressure of bed (%)
Before	0.75	0.151	0.02
After	0.70	0.13	0.01

7. Wave and mud interaction

To investigate the model's capability in the simulation of waves interacting with mud, a wave propagation over non-Newtonian mud was simulated. A schematic diagram of the water and mud layers in the simulation of wave-mud interaction is displayed in Figure 8. The sinusoidal waves were produced using a piston wave maker at the inlet of a flume with a length of 10 m [3]. To prevent the adverse effects of wave reflection from the flume end, an exponential function was used as a numerical wave absorber in this area. The water depth used in the present study varied from 0.2 to 0.3 m, and the mud depth varied from 0.06 to 0.11 m. The time step and the initial particle spacing were equal to 0.001s and 0.01 m, respectively. The whole number of particles varied from 30000 to 40000 depending on the depth of water and mud layers. The water was regarded as Newtonian fluid, and the non-Newtonian fluid with the Bingham plastic model was adopted for mud rheology [3]. The water viscosity and density were set to 10^{-6} m^2/s and 1000 kg/m^3 respectively. Several simulations have been carried out to

make comparisons with the experimental results of [4-7]. The rheological parameters for each mud were obtained from the rheometric tests reported in their studies.

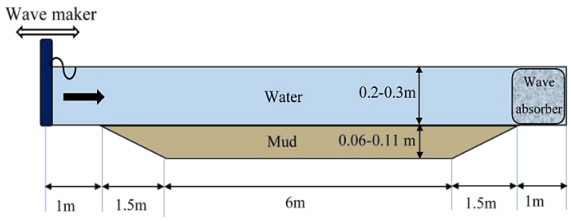

Fig. 8: Schematic diagram of water and mud layers in the simulation of wave and mud interaction

Snapshots of wave and mud interaction, along with pressure contours, are shown at different times in Figure 9. In this figure, when the wave propagates over the mud layer, the wave height decreases, but the wave length increases. The contours of pressure display the maximum values within the mud layer, particularly near the bottom under the wave crest.

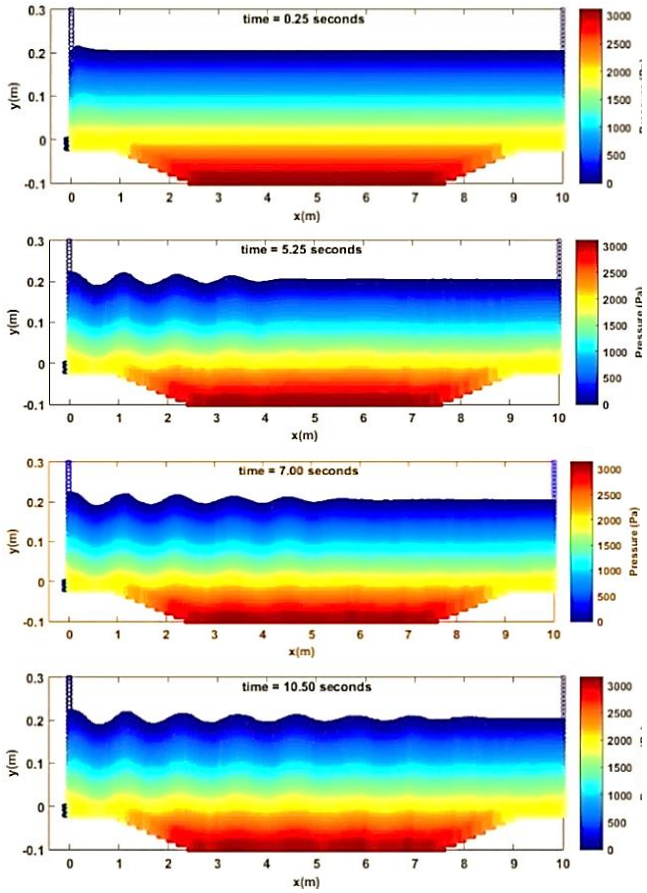

Fig. 9: Snapshots of simulated wave-mud interaction and contours of pressure (Pa) at different times; H=4 cm and mud density=1240 kg/m^3

8. Results and discussion

8.1 Attenuation of wave

The wave height (H) along the muddy bed (x) is related to the initial wave height (H_0) and dissipation rate of the wave (attenuation coefficient) (k_i) as follows [35]:

$$H = H_0 \, e^{-k_i \, x} \tag{45}$$

Using equation 45, the dissipation rate is determined by calculating the slope of the line best fitted to the data belonging to the highest points of the wave crests. Table 2 shows the results of the dissipation rate for the present model with approaches I (conventional pairwise calculation of the shear rates magnitude of the particle i with each j particle) and II (calculate simultaneously the effect of all neighboring particles (j) inside the support domain) in the calculation of shear stress as mentioned in section 5.1 and their comparison with the experimental results of Sakakiyama and Bijker (SB) [4]. Although both approaches give acceptable results, the relative errors of the new approach (II) are less than those of approach (I) indicating the positive effect of the new formulation on the calculation of shear stress. It seems that the approach (I) overestimates the shear stress and results in more wave attenuation in comparison to the approach (II).

Figure 10 shows the predicted dissipation rate of two waves with and without the interface treatment compared with the experimental results. The predicted values of both cases agree well with the measured ones. However, the modified interface treatment enhances the simulation, resulting in better results than without the modified treatment. It seems that the modification in the formulations of shear stress and interface treatment together makes a better transfer of force and energy from the surface wave into the muddy bed and also handles the discontinuity in the pressure gradient across the interface. The investigation of the simulated attenuation rates indicates there was little overestimation compared to the measurements. This can be attributed to the intrinsic characteristic of the SPH method that causes some inbuilt dissipation.

8.2 Mud mass transport velocities

Experimental results demonstrate that the mud transport inside the mud layer is more dominant than the transport of suspended mud in the water layer under wave actions [36]. Tracking the position of each particle at any time can be easy due to the Lagrangian and particle-based properties of SPH. A comparison between the simulated (the current model and the model reported by Hejazi et al. [3]) and the measurement of mud mass transport velocity [7] over the mud layer depth is provided in Figure 11. The present simulated values agree well with the measurements conducted by Soltanpour et al. [7] both in magnitude and distribution of the mud mass transport velocity in comparison to the results of [3]. However, there are some discrepancies between the two results that may be attributed to the use of simplified rheology for mud in the numerical model. Wave height strongly affects the mud mass transport velocity. For example, a growth of 2 cm in the wave height causes the mass transport velocity to increase twice. Therefore,

Consistent with the experimental results, it may be stated that mass transport velocity is related to wave height having power higher than 2 [4]. As wave height increases, it exerts a comparatively larger driving force to move mud, resulting in a larger mud mass transport velocity. Both the present numerical and experimental [7] results show non-uniform mud mass transport velocity over depth, contrary to results of Sakakiyama and Bijker [4].

Table 2: wave attenuation coefficient (k_i); the ISPH model with both approaches compared with the experimental results and the corresponding relative errors [4]

Test no.	Wave and mud properties			k_i (1/m)			RE (%) of k_i (1/m)	
				Experimental	Numerical			
	H_0 (cm)	T (s)	ρ (kg/m^3)	[4]	approach I	approach II	approach I	approach II
1	4	1.0	1370	0.183	0.191	0.189	4.3	3.3
2	3.2	0.8	1300	0.068	0.080	0.078	17.6	14.7
3	3.2	1.0	1300	0.084	0.086	0.085	2.4	1.2
4	2.8	~0.8	1240	0.031	0.034	0.034	9.7	9.7
5	2.8	~0.7	1300	0.068	0.0725	0.072	6.6	5.9
6	~2	0.7	1300	~0.1	0.109	0.108	9.0	8.0

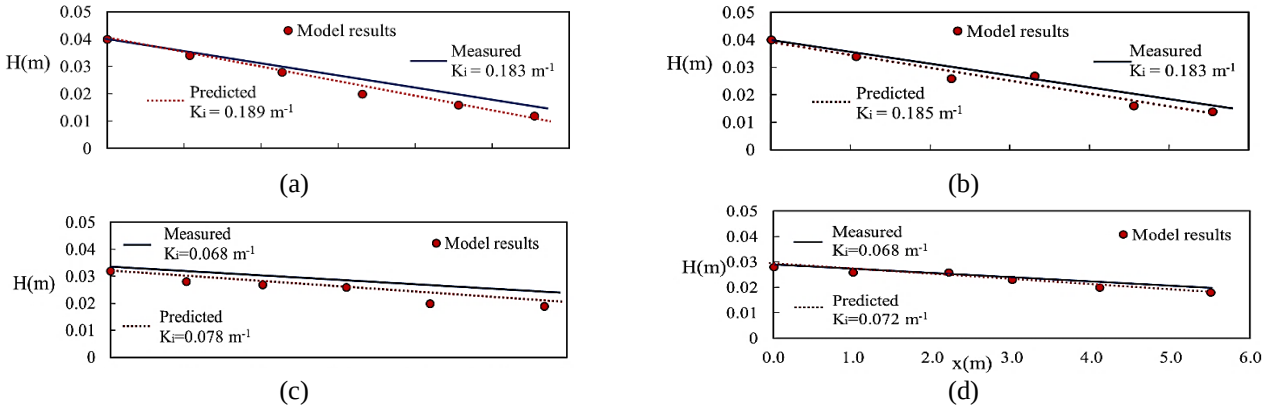

Fig. 10: Wave dissipation rates; model results compared with measurements [4], (a, b) H_0=4 cm, Wave Period =1s, Mud density=1370 kg/m^3; (c, d) H_0=3.2 cm, Wave Period ≈0.8s Mud density=1300 kg/m^3; (a, c) without modification, (b, d) with modification in interface

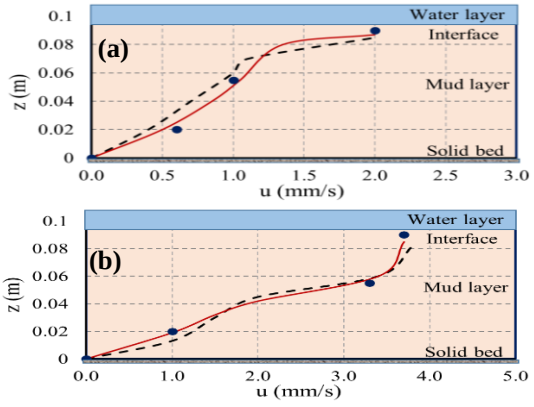

Fig. 11: Comparisons between the experimental [7] (almond shapes), present simulated results (red lines) and the model of Hejazi et al. [3] (dashed lines) of mud mass transport velocity; a) T=1.1 s, H=5 cm; b), T=1.1 s, H=7.0 cm, mud density=1300 kg/m^3

Figure 12 displays the simulated mud mass transport velocities at the water and mud interface with respect to the different heights of the free-surface waves for three wave periods compared with the laboratory results [4]. Consistent with the experimental data, it is distinct that longer waves or higher periods, and higher wave heights cause larger mass transport velocities.

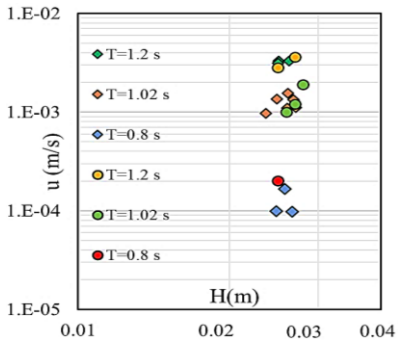

Fig.12: Relationship between mud mass transport velocity, wave heights, and periods at the interface; comparison of the ISPH model (circles) with experimental results [4] (diamonds)

9. Conclusions

In this study, the ISPH model of Hejazi et al. [3] was developed using the interparticle average method in the entire domain. Free surface relationships were extracted for this method. Correction coefficients were presented for the relations between water and soil interface, which increase the accuracy of the interface position. Also, a new approach in calculating shear stress was presented. The simulation of sinusoidal and solitary wave propagation showed good agreement with the analytical solutions. The attenuation of wave height passing over the mud layer and the velocity of mud mass transport have been investigated. The modifications made increased the accuracy of the results of the current modified ISPH model compared to the model of Hejazi et al. [3]. The main results are as follows:

1. The iterative projection method used in the current model increased the accuracy of both the velocity and density of the particles due to enforcing full incompressibility.
2. The simulated results showed that wave lengthens, and wave height decreases over the mud layer.
3. Over the muddy layer, as the density of mud increases, the dissipation rate of the wave also increases.
4. The results showed that the magnitude of mass transport velocities depends significantly on both wave height and period.
5. The results showed a direct relationship between wave attenuation and mud mass transport.T his indicates that high mass transport requires high energy consumption.
6. The mud mass transport velocity near the interface showed a relatively great difference from within the mud layer.
7. The use of the modifications in the new ISPH improved the force and energy transfer from the surface wave into the fluid mud, and it enhanced the simulated results in terms of the particle position, pressure field, dissipation rate, and mud mass transport velocity.
8. Although the present numerical model demonstrated acceptable simulated results, it has some restrictions, such as being 2D, using the simple Bingham rheological model, and considering mud as a fluid. Due to the environmental and structural significance of the mass transport and wave attenuation resulting from the wave mud interaction, it would be better to simulate nonlinear waves with other rheological models and different bed geometries with the robust ISPH model. The incorporation of a turbulence model and considering mud as a granular material, as well as theextension of the present model to 3D, can enhance the model's capabilities.

References

[1] Samsami, F., Haghshenas, S. A., Soltanpour, M., 2022. Physical and rheological characteristics of sediment for nautical depth assessment in Bushehr Port and its access channel. Water, 14 (24), 4116, https://doi.org/10.3390/w14244116.

[2] Li, W., Li, M., Zhang, X., Li, J. (2023). Characteristics of fluid mud in the Yangtze Estuary: Storm, tide, and slope-triggered sediment dynamics and effects, Estuarine. Coastal and Shelf Science, 281, 108194. https://doi.org/10.1016/j.ecss.2022.108194.

[3] Hejazi, K., Soltanpour, M., Aslani Kordkandi, A. (2023). An incompressible SPH numerical model for simulating wave and non-Newtonian mud interaction. Coastal Engineering 185 104379. doi.org/10.1016/j.coastaleng.2023.104379.

[4] Sakakiyama, T., Bijker, E.W. (1989). Mass transport velocity in mud layer due to progressive waves. J. Waterway Port Coast Ocean Eng. ASCE, 115 (5), 614–633.

[5] Soltanpour, M., Samsami, F. (2011). A comparative study on the rheology and wave dissipation of kaolinite and natural Hendijan Coast mud. the Persian Gulf. Ocean Dynamics, 61, 295–309.

[6] Hsu, W.Y., Wung, H.H., Hsu, T.J., Torres–Freyermuth, A., Yang, R.Y. (2013). An experimental and numerical investigation on wave–mud interactions. J. Geophys. Res. Oceans, 118, 1126–1141.

[7] Soltanpour, M., Shamsnia, S.H., Shibayama, T., Nakamura, R. (2018). A study on mud particle velocities and mass transport in wave–current–mud. Applied Ocean Research, 78, 267–280.

[8] Shamsnia, S.H., Soltanpour, M., Bavandpour, M., Gualtieri, C. (2019). A Study of Wave Dissipation Rate and Particles Velocity in Muddy Beds. Geosciences, 9, 212. https://doi.org/10.3390/geosciences9050212.

[9] Soltanpour, M., Shamsnia, S.H., Shibayama, T. et al. (2020). Experimental and analytical investigation of the response of a mud layer to solitary waves. Ocean Dynamics 70, 165–186. https://doi.org/10.1007/s10236-019-01319-6.

[10] Quesada, A., Bautista, E., Méndez, F. (2022). Damping coefficient by long waves-viscoelastic mud–current interaction. Physics of Fluids 34, (9). https://doi.org/10.1063/5.0098055.

[11] Mahshid, K., Ghader, S., Shamsnia, S.H. et al. (2022). An analytical solution to wave dissipation induced by interacting waves and currents with muddy deposits. Ocean Dynamics 72, 715–730. https://doi.org/10.1007/s10236-022-01526-8.

[12] Hejazi, K., Soltanpour, M., Sami, S. (2013). Numerical modeling of wave–mud interaction using projection method. Ocean Dynamics, 63, 1093–1111.

[13] Zainali A., Tofighi N., Shadloo M.S, Yildiz M. (2013). Numerical investigation of Newtonian and non-Newtonian multi-phase Flows Using ISPH Method. Comput Meth Appl Mech Eng, 254, 99–113.

[14] Monaghan, J.J., Rafiee, A. (2013). A simple SPH algorithm for multi–fluid flow with high density ratios. Int. J. Numer. Meth. In Fluids, 71, 537–561.

[15] Hu, X.Y., Adams, N.A. (2007). An incompressible multi–phase SPH method. Journal of Computational Physics, 227, 264–278.

[16] Hu, X.Y., Adams, N.A. (2009). A constant–density approach for incompressible multi–phase SPH. Journal of Computational Physics, 228 (6), 2082 – 2091.

[17] Harada, E., H., Ikari, Tazaki, T., Gotoh, H. (2021). Numerical simulation for coastal morphodynamics using DEM-MPS method. Applied Ocean Research 117(9),102905. DOI: 10.1016/j.apor.2021.102905.

[18] Tsurudome, C., Liang, D., Shimizu, Y., Khayyer, A., Gotoh, H. (2021). Study of beach permeability's influence on solitary wave runup with ISPH method. Applied Ocean Research, 117,102957.

[19] Mao, Y., Kong, Y., Guan, M. (2022). GPU-accelerated SPH modelling of flow-driven sediment erosion with different rheological models and yield criteria. Powder Technology, 412, 118015.

[20] Tazaki, T., Harada, E., Gotoh, H. (2023). Grain-scale investigation of swash zone sediment transport on a gravel beach using DEM-MPS coupled scheme. Coastal Engineering Journal, 65(2), 347–368.

[21] Xu, F., Wang, J., Yang, Y., Wang, L., Dai, Z., Han, R. (2023). On methodology and application of smoothed particle hydrodynamics in fluid, solid and biomechanics. Acta Mech. Sin., 39, 722185. https://doi.org/10.1007/ s10409-022-22185-x .

[22] Nabian, M. A., Farhadi, L. (2017). Multiphase mesh-free particle method for simulating granular flows and sediment transport. Journal of Hydraulic Engineering, 143(4), 4016102.

[23] Wang, L., Jiang, Q., Khayyer, A., Zhang, C. (2019). A multiphase particle method for interaction between sluicing water and fluvial mud beds. Proceedings of the Twenty-ninth International Ocean and Polar Engineering Conference.

[24] Han, Z., Su, B., Li, Y., Wang, W., Wang, W., Huang, J., Chen, G. (2019). Numerical simulation of debris-flow behavior based on the SPH method incorporating the Herschel-Bulkley-Papanastasiou rheology model. Engineering Geology, 225, 26-36.

[25] Shao, S., Lo, E.Y.M. (2003). Incompressible SPH method for simulating Newtonian and non–Newtonian flows with a free surface. Advances in water resources, 26 (7), 787–800.

[26] Monaghan, J.J. (2005). Smoothed particle hydrodynamics, Reports on Progress in Physics, 68, 1703–1759.

[27] Kruisbrink, A., Korzilius, S., Pearce, F., Morvan, H. (2018). SPH particle collisions for the reduction of particle clustering, interface stabilisation and wall modelling. Journal of Applied Mathematics and Physics, 6 (9), DOI: 10.4236/jamp.2018.69158.

[28] Ataie-Ashtiani, B., Shobeiry, G., Farhadi, L. (2008). Modified incompressible SPH method for simulating free surface problems. Fluid Dynamic Research, 40, 637–661.

[29] Chen, Z., Zong, Z., Liu, M.B., Zou, L., Li, H.T., Shu, C. (2015). An SPH model for multiphase flows with complex interfaces and large density differences. Journal of Computational Physics, 283, 169–188.

[30] Khayyer, A., Gotoh, H., Shao, S. (2008). Corrected Incompressible SPH method for accurate water-surface tracking in breaking waves. Coastal Engineering, 55, 236-250.

[31] Papanastasiou, T.C. (1987). Flows of materials with yield. journal of rheology, 31, 385-404. https://doi.org/10.1122/1.549926.

[32] Bonet, J., Lok, T.S. (1999). Variational and momentum preservation aspects of smooth particle hydrodynamic formulation. Comput. Methods Appl. Mech. Eng., 180 (1-2), 97–115.

[33] Lee J.J. et al. (1982). Measurement of velocities in solitary waves. J. Waterway Port, Coast Ocean Div, ASCE 108 (2). https://doi.org/10.1061/JWPCDX.0000293.

[34] Dean R.G., Dalrymple R.A. (1991). Water Wave Mechanics for Engineers and Scientists. Prentice-Hall, Englewood Cliffs, NJ.

[35] Iwasaki T., Sato M. (1972). Dissipation of wave energy due to opposing current. Proc. 13th Coastal Eng. Conf., ASCE, 1, 605–622.

[36] Shibayama T., Okuno M., Sato S. (1990). Mud transport rate in mud layer due to wave action. Proc. Coast. Eng., ASCE, 3037–3049.